APPLIED PHYSICS

Near-infrared and visible light dual-mode organic photodetectors

Zhaojue Lan[1,2], Yanlian Lei[1], Wing Kin Edward Chan[1], Shuming Chen[2], Dan Luo[2]*, Furong Zhu[1]*

We report a dual-mode organic photodetector (OPD) that has a trilayer visible light absorber/optical spacer/near-infrared (NIR) light absorber configuration. In the presence of NIR light, photocurrent is produced in the NIR light–absorbing layer due to the trap-assisted charge injection at the organic/cathode interface at a reverse bias. In the presence of visible light, photocurrent is produced in the visible light–absorbing layer, enabled by the trap-assisted charge injection at the anode/organic interface at a forward bias. A high responsivity of >10 A/W is obtained in both short and long wavelengths. The dual-mode OPD exhibits an NIR light response operated at a reverse bias and a visible light response operated at a forward bias, with a high specific detectivity of ~10^{13} Jones in both NIR and visible light ranges. A bias-switchable spectral response OPD offers an attractive option for applications in environmental pollution detection, bioimaging process, wellness, and security monitoring in two distinct bands.

INTRODUCTION

Organic photodetectors (OPDs) are a promising alternative optical detecting technology to conventional inorganic counterparts because the optical and electric properties of organic semiconducting materials can be tailored accordingly (*1*). They offer additional advantages such as having a solution-processable fabrication process, which also leads to substantial cost-benefits, thereby creating next-generation solution-processable, flexible, and low-cost photodetectors (*2*). In general, the spectral responses of the photodetectors are determined by the absorption of the active materials and optical profile in the devices (*3*). Discrete OPDs using organic semiconductors with different optical bandgaps for x-ray and ultraviolet (UV), visible, near-infrared (NIR) light detections have been reported (*4*–*6*). Recently, a high-performing, solution-processable NIR light to visible light up-conversion organic/perovskite hybrid device, comprising an NIR OPD unit and a perovskite light-emitting emitter, has been demonstrated for visualizing the NIR light (*6*). OPDs with different spectral responses can be realized using different approaches of optical microcavity (*7*), charge collection narrowing (CCN) (*8*–*10*), and intermolecular charge transport absorption (*11*). Filter-free OPDs with a narrowband photoresponse in a well-defined wavelength range were obtained by incorporating a thick light-absorbing layer, realizing visible narrowband OPDs with a full width at half maximum of ~30 nm (*12*). NIR narrowband OPDs were demonstrated using microcavity effect and enhanced intermolecular charge transport absorption in organic semiconductors (*13*). These achievements, however, are made with the single-mode OPDs optimized for photodetection at the specific wavelengths. The progress made in dual-mode or multimode OPDs that have simultaneous photoresponses to different wavelength ranges is less impressive.

Realizing spectral tunable OPDs with high detectivity in two distinct bands, particularly over the wavelength range from NIR and visible light, is very attractive for a plethora of applications in environmental pollution detection, bioimaging process, wellness, security monitoring, etc. However, reports on spectral tunable OPDs are rather rare. A UV OPD with distinguishable difference in peak spectral responses located at 365 and 330 nm was observed when its transparent indium tin oxide (ITO) anode and the semitransparent cathode of Al (15 nm)/Ag (100 nm) were exposed to the incident light (*4*) due to the respective absorptions of the donor and acceptor in the planar donor/acceptor heterojunction. Different spectral responses, e.g., exhibiting broadband and narrowband characteristics due to the CCN effect, were also observed in a thick perovskite photodetector when its top side or bottom side was exposed to the incident light (*14*). Spectral tunable OPDs that can be operated without flipping the detectors are of practical interests.

The photomultiplication (PM) effect was demonstrated in the OPD with a binary heterojunction layer having a weight ratio of poly(3-hexylthiophene-2,5-diyl) (P3HT) to [6,6]-phenyl-C70 butyric acid methyl ester ($PC_{70}BM$) of 100:1 (*15*, *16*). It is shown that the electron traps, formed due to the presence of a very low amount of $PC_{70}BM$ in the binary blend P3HT:$PC_{70}BM$ active layer, assists in enhancing hole injection in the OPDs, resulting in high external quantum efficiency (EQE) over 100% (*17*). The spectral response behavior in PM OPDs can be controlled by adjusting the charge injection properties via carrier tunneling effect at the anode/organic and organic/cathode interfaces (*18*, *19*). These OPDs having different spectral responses, tuning from the narrowband to broadband in the well-defined spectral ranges, were obtained by modulating the applied bias. Dual-mode OPDs with a unique tunable photodetection capability, particularly over the NIR and visible light wavelength ranges, that can be operated by adjusting the polarity of the biases are still an open challenge.

In this work, we report our effort to develop a dual-mode OPD that has an NIR light response operated at a reverse bias and a visible light response operated at a forward bias. The bias-switchable spectral response OPD has a layer configuration comprising ITO/polyelectrolyte, poly[(9,9-bis(3′-((*N*,*N*-dimethyl)-*N*-ethylammonium)-propyl)-2,7-fluorene)-alt-2,7-9,9-dioctylfluoren)] dibromide (PFN-Br)/binary blend P3HT:$PC_{70}BM$ visible light absorber/pristine P3HT optical spacer/ternary blend P3HT:poly[4,8-bis(5-(2-ethylhexyl)thiophen-2-yl)benzo[1,2-b;4,5-b′]dithiophene-2,6-diyl-alt-(4-(2-ethylhexyl)-3-fluorothieno[3,4-b] thiophene-)-2-carboxylate-2-6-diyl)] (PTB7-Th):$PC_{70}BM$ NIR light absorber/aluminum (Al). This is the first type of

[1]Department of Physics, Research Centre of Excellence for Organic Electronics, Institute of Advanced Materials, and State Key Laboratory of Environmental and Biological Analysis, Hong Kong Baptist University, Kowloon Tong, Hong Kong, China. [2]Department of Electrical and Electronic Engineering, Southern University of Science and Technology, Shenzhen 518055, China.
*Corresponding author. Email: luod@sustc.edu.cn (D.L.); frzhu@hkbu.edu.hk (F.Z.)

dual-mode OPD that can be operated in both reverse and forward biases for attaining high photoresponses in NIR and visible light wavelength ranges.

RESULTS

Dual-mode OPD

Before the study of the dual-mode OPD, the spectral response behaviors of a PM OPD with a binary blend P3HT:$PC_{70}BM$ single-active layer, having a weight ratio of P3HT to $PC_{70}BM$ of 100:1, operated at a reverse bias and a forward bias were analyzed. The distribution of a low $PC_{70}BM$ concentration forms the $PC_{70}BM$-induced electron traps across the binary blend P3HT:$PC_{70}BM$ (100:1) active layer in the PM OPD. The PM OPD has a layer configuration comprising ITO/PFN-Br/P3HT:$PC_{70}BM$ (100:1) (300 nm)/Al. The PM OPD with a 300-nm-thick P3HT:$PC_{70}BM$ (100:1) active layer has an EQE of 700% operated at a reverse bias of −6 V, and an EQE of 3600% was obtained for the PM OPD operated at a forward bias of 6 V, as shown in Fig. 1 (A and B). At a reverse bias, the PM OPD responds only to the short-wavelength light (with a peak response near 380 nm) and long-wavelength light (with a peak wavelength near 620 nm), as shown in Fig. 1A. At a forward bias, however, the PM OPD has a broadband response over the wavelength range from 300 to 650 nm. Such a bias polarity–dependent spectral response of the PM OPD is closely associated with the difference in the wavelength-dependent light absorption in the PM OPD.

The depth profile of the wavelength-dependent light absorption in the P3HT:$PC_{70}BM$ (100:1)–based PM OPD is shown in Fig. 1C. It reveals that the incidence of light with a broad wavelength range from 300 to 650 nm is absorbed near the vicinity of the anode/organic side, while relatively stronger absorption over the short-wavelength and long-wavelength ranges appears near the organic/cathode interface in the PM OPD. The inset in Fig. 1A illustrates the existence of band bending, induced by the accumulation of the photogenerated electrons due to the absorption of the short- and long-wavelength photons near the vicinity of the organic/cathode interface. Therefore, the tunneling hole injection process occurs at the organic/cathode interface in OPD when it is operated at a reverse bias. The inset in Fig. 1B illustrates the presence of the band bending near the vicinity of the anode/organic interface, induced by the accumulation of the photogenerated electrons due to the absorption of the broadband photons. This leads to the tunneling hole injection process to take place at the anode/organic interface in OPD when it is operated at a forward bias. The analysis made with the depth profile of the optical absorption distribution in Fig. 1C agrees well with the EQE spectra measured for the PM OPD at the reverse and forward biases, as shown in Fig. 1 (A and B). The similar bias polarity–dependent spectral response is also observed in a PM OPD with a 2.0-μm-thick ternary blend P3HT:PTB7-Th:$PC_{70}BM$ single-active layer, having a weight ratio of P3HT to PTB7-Th to $PC_{70}BM$ of 70:30:1, operated at the reverse and forward biases, as shown fig. S1.

A high-performance dual-mode OPD with a unique feature of high NIR light response, operated at a reverse bias, and visible light response, operated at a forward bias, has been demonstrated. The dual-mode OPD, e.g., with a layer configuration comprising ITO/PFN-Br/P3HT:$PC_{70}BM$ (100:1) (visible light–absorbing layer)/P3HT (optical spacer)/P3HT:PTB7-Th:$PC_{70}BM$ (70:30:1) (NIR light–absorbing layer)/Al, has a unique feature of NIR light response over the wavelength range from 630 to 800 nm, operated at a reverse bias, and visible light response over a wavelength range from 310 to 650 nm, operated at a forward bias. The cross-sectional view of a dual-mode OPD with a trilayer configuration active layer of P3HT:$PC_{70}BM$

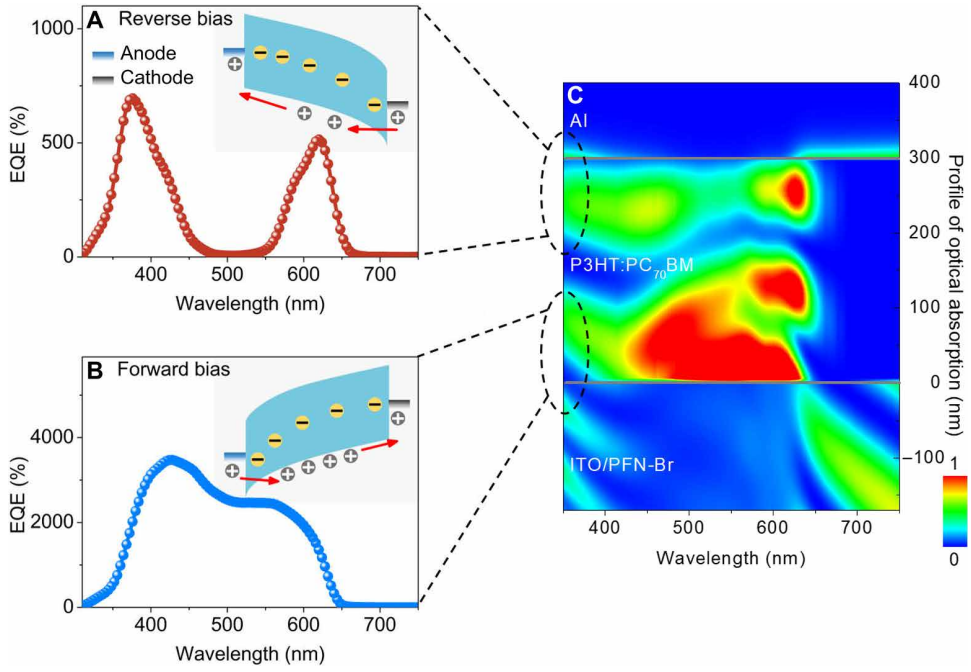

Fig. 1. P3HT:$PC_{70}BM$ (100:1)-based PM OPD. EQE spectra measured for the PM OPD at (**A**) a reverse bias of −6 V and (**B**) a forward bias of 6 V. (**C**) Distribution of photogenerated electrons in a 300-nm-thick P3HT:$PC_{70}BM$ (100:1)–based PM OPD. The inset in (A) illustrates the existence of the band bending and tunneling hole injection process at the organic/cathode interface in OPD operated at a reverse bias. The inset in (B) illustrates the presence of the band bending and tunneling hole injection process at the anode/organic interface in OPD operated at a forward bias.

(100:1) (300 nm) visible light absorber/P3HT (320 nm) optical spacer/P3HT:PTB7-Th:$PC_{70}BM$ (70:30:1) (500 nm) NIR light absorber is shown in the inset in Fig. 2A. The normalized absorption spectra measured for a 300-nm-thick binary blend P3HT:$PC_{70}BM$ (100:1) layer, a 320-nm-thick pristine P3HT layer, and a 500-nm-thick ternary blend P3HT:PTB7-Th:$PC_{70}BM$ (70:30:1) layer are plotted in Fig. 2A. Compared to the absorption spectra measured for the pristine P3HT and binary blend P3HT: $PC_{70}BM$ (100:1) layers, it is clear that the ternary blend P3HT:PTB7-Th:$PC_{70}BM$ (70:30:1) film has an obvious extended absorption in the NIR light over the wavelength range from 650 to 800 nm. The absorption spectra calculated for a 300-nm-thick binary blend P3HT:$PC_{70}BM$ (100:1) visible light–absorbing layer, a 320-nm-thick pristine P3HT optical spacer, and a 500-nm-thick ternary blend P3HT:PTB7-Th:$PC_{70}BM$ (70:30:1) NIR light–absorbing layer in the OPD are plotted in Fig. 2B. The schematic energy level diagram of the corresponding functional materials used in the dual-mode OPDs is shown in fig. S2.

The optical field distribution and profile of charge generation distribution in the dual-mode OPD, with a layer configuration comprising ITO/PFN-Br/P3HT:$PC_{70}BM$ (100:1) (300 nm)/P3HT (320 nm)/P3HT:PTB7-Th:$PC_{70}BM$ (70:30:1) (500 nm)/Al (100 nm), were calculated using the optical admittance analysis (*20*, *21*). The optical field distribution across the binary blend P3HT:$PC_{70}BM$ (100:1) (300 nm) visible light–absorbing layer, pristine P3HT (320 nm) optical spacer, and ternary blend P3HT:PTB7-Th:$PC_{70}BM$ (70:30:1) (500 nm) NIR light–absorbing layer in the dual-mode OPD as a function of the wavelength is shown in Fig. 3A, revealing the profile of the wavelength-dependent light intensity in the OPD. Figure 3A reveals that the incident light with wavelength >650 nm can only be absorbed in the 500-nm-thick ternary blend P3HT:PTB7-Th:$PC_{70}BM$ (70:30:1) layer in the OPD. The normalized distribution of the photogenerated charge carriers across the P3HT:$PC_{70}BM$ (100:1) visible light–absorbing layer, pristine P3HT optical spacer, and P3HT:PTB7-Th:$PC_{70}BM$ (70:30:1) NIR light–absorbing layer as a function of the wavelength is shown in Fig. 3B. It becomes clear that the incident light with wavelengths shorter than 650 nm is mainly absorbed by the 300-nm-thick binary blend P3HT:$PC_{70}BM$ (100:1) layer. The 320-nm-thick pristine P3HT layer acts as an optical spacer to deplete the visible light that is not fully absorbed by the binary blend P3HT:$PC_{70}BM$ (100:1) layer, allowing the long-wavelength light to reach the ternary blend P3HT:PTB7-Th:$PC_{70}BM$ (70:30:1) layer. The optical field distribution and profile of the photogenerated charge carriers calculated for the OPD at two different wavelengths of 460 and 770 nm are plotted in Fig. 3 (C and D). It is clear that the photo charge carriers generated by the 460-nm light are mainly retained within the 300-nm-thick binary blend P3HT:$PC_{70}BM$ (100:1) visible light–absorbing layer. The short-wavelength light (460 nm) is fully depleted by the 320-nm-thick pristine P3HT optical spacer layer. The simulation results show that the NIR light, e.g., with a wavelength of 770 nm, penetrates through the binary blend P3HT:$PC_{70}BM$ (100:1) visible light–absorbing layer and P3HT optical spacer to generate the photo charge carriers in the 500-nm-thick ternary blend P3HT:PTB7-Th:$PC_{70}BM$ (70:30:1) NIR light–absorbing layer.

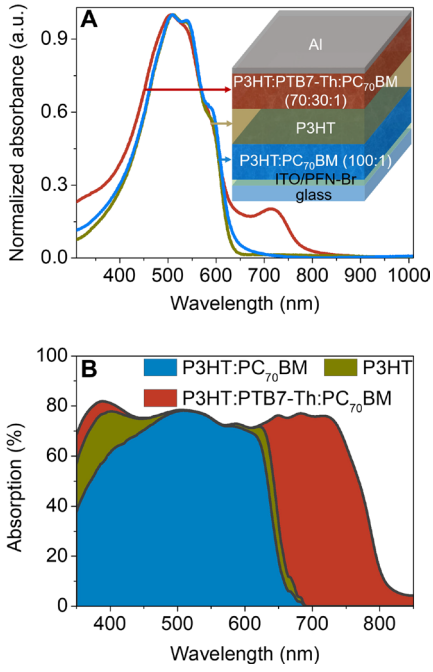

Fig. 2. Device configuration and absorption distribution. (**A**) Normalized absorption spectra measured for a binary blend P3HT:$PC_{70}BM$ (100:1) layer, a pristine P3HT layer, and a ternary blend P3HT:PTB7-Th:$PC_{70}BM$ (70:30:1) layer. Inset: Schematic diagram illustrating the cross-sectional view of the OPD, having a layer configuration comprising ITO/PFN-Br/P3HT:$PC_{70}BM$ (300 nm)/P3HT (320 nm)/P3HT:PTB7-Th:$PC_{70}BM$ (500 nm)/Al. a.u., arbitrary unit. (**B**) The absorption spectra calculated for 300-nm-thick binary blend P3HT:$PC_{70}BM$ (100:1), 320-nm-thick pristine P3HT, and 500-nm-thick ternary blend P3HT:PTB7-Th:$PC_{70}BM$ (70:30:1) layers.

NIR and visible light dual-mode photo responses

The current-voltage (*I-V*) characteristics of the dual-mode OPD in the presence of NIR light (770 nm), measured by scanning from −35 to 15 V, are plotted in Fig. 4A. *I-V* characteristics of the dual-mode OPD in the visible light (460 nm), measured by scanning from 15 to −35 V, are plotted in Fig. 4B. In Fig. 4A, a significant photocurrent was obtained for the reverse-biased OPD in the presence of the NIR light. The photocurrent density of the OPD increases with the reverse bias. The bias-switchable spectral response OPD remained an almost constant current density when it was operated at different forward biases (in the visible light detection mode) in the presence of the NIR light. In the presence of the visible light, the strong photoresponses were observed for the OPD operated at the different forward biases, remaining a similar low-current density when the OPD was at different reverse biases (in the NIR light detection mode), as shown in Fig. 4B. The dual-mode OPD with a unique feature of high NIR light response, operated at a reverse bias, and visible light response, operated at a forward bias, is demonstrated.

The responsivities (in A/W) measured for the dual-mode OPD operated at the NIR light mode (at different reverse biases) and visible light mode (at different forward biases) are shown in Fig. 4C. It can be seen that the dual-mode OPD has different spectral responses when it is operated under the forward and reverse biases. The dual-mode OPD responds over the wavelength range from 310 to 650 nm when it is operated at a forward bias. The dual-mode OPD responds primarily over the wavelength range from 630 to 800 nm operated at a reverse bias. Benefiting from the PM effect, a responsivity of 8.66 A/W was realized for the NIR mode of the OPD operated at −40 V. A peak responsivity of 7.47 A/W was obtained for the dual-mode OPD in the presence of the visible light operated at a forward bias of 15 V. EQE spectra measured for the dual-mode OPD operated in the NIR light detection mode, at different reverse biases of −30, −35, and −40 V, and

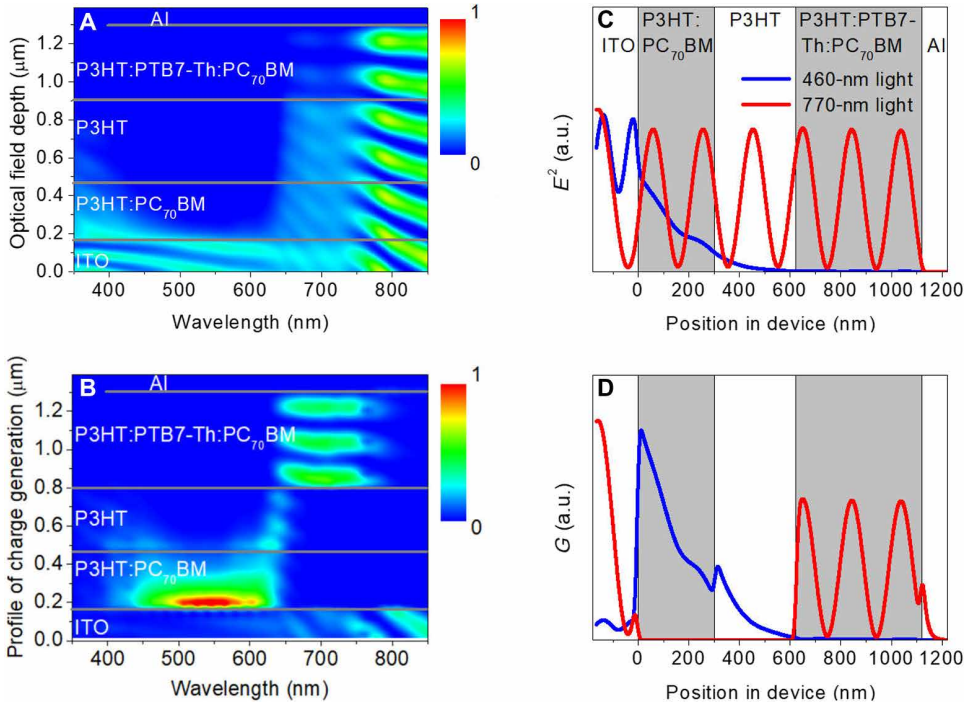

Fig. 3. Optical simulation. (**A**) Simulated optical field distribution and (**B**) the normalized photogenerated electron distribution across the 300-nm-thick binary blend P3HT:$PC_{70}BM$ (100:1) visible light–absorbing layer, 320-nm-thick pristine P3HT optical spacer layer, and 500-nm-thick ternary blend P3HT:PTB7-Th:$PC_{70}BM$ (70:30:1) NIR light–absorbing layer in the dual-mode OPD. (**C**) Optical field distribution and (**D**) profile of the photogenerated charge carriers calculated for the dual-mode OPD at two different wavelengths of 460 and 770 nm.

in the visible light detection mode, at forward biases of 9, 12, and 15 V, are presented in fig. S3 (A and B). The results in fig. S3 (A and B) show that an EQE of 1643% was realized for the NIR mode of the OPD operated at −40 V, and an EQE of 2465% was obtained for the OPD operated at 15 V.

The specific detectivity (D^*) of the dual-mode OPD was also analyzed, which is closely associated with EQE and noise current. The noise current in OPDs includes the shot noise, thermal noise, 1/f noise, and generation-recombination noise (*22*). In the PM OPD, the noise current is dependent on the shot noise and thermal noise (*23*). The shot noise can be calculated using the following equation

$$i_{shot} = \sqrt{2eI_{dark}B} \quad (1)$$

where B is the normalized bandwidth. The performance repeatability of the dual-mode OPD was evaluated by repeating the I-V characteristic measurements continuously for more than seven times, and the average of the measured results is plotted in Fig. 4D, indicating a good repeatability and stability of the I-V characteristics. The I_{dark} of the dual-mode OPD is 7.39×10^{-8} A at 10 V, corresponding to an i_{shot} of about 1.54×10^{-13} A/$Hz^{0.5}$. The thermal noise of the dual-mode OPD is related to its shunt resistance, R_{sh}, and it can be expressed by

$$i_{thermal} = \sqrt{\frac{4kTB}{R_{sh}}} \quad (2)$$

where T is the temperature in kelvin. The impedance spectrum measured for the OPD is plotted in Fig. 4E, revealing the dual-mode OPD having a shunt resistant of 23.4 megohms measured at 10 V (*22*). At room temperature, e.g., T = 298 K, the thermal noise of the OPD is 2.65×10^{-14} A/$Hz^{0.5}$. It is clear that the shot noise is about six times higher than the thermal noise. Therefore, the shot noise is used to calculate for D^* as an approximation using the following equation

$$D^* = \frac{EQE \cdot e \cdot \lambda}{hc \cdot \sqrt{2e \cdot J_{dark}}} (Jones) \quad (3)$$

where J_{dark} is the dark current density and c is the speed of light. The D^* as a function of the wavelength obtained for the dual-mode OPD in the NIR and visible light detection modes operated at different reverse and forward biases are plotted in Fig. 4F. The dual-mode OPD with a high D^* of ~10^{13} Jones was obtained in the presence of the NIR and visible light, revealing the dual-mode OPD with comparable high performance for both NIR and visible light detection. D^* of the dual-mode OPD in the NIR light detection mode increases with the decrease in the reverse bias from −35 to −40 V, and that for the dual-mode OPD in the visible light detection mode increases with forward bias from 12 to 15 V, realized by the markedly enhanced photocurrent and low dark current in the dual-mode OPD.

A summary of the dark current, responsivity, EQE, and D^*, measured for the dual-mode OPD operated at different reverse and forward biases, using a short-wavelength (376 nm) and a long-wavelength (654 nm) light source, is listed in table S1. A high responsivity of 14.44 A/W, EQE of 4767%, and a high D^* of 1.40×10^{13} Jones were obtained for the dual-mode OPD in the presence of short wavelength, e.g., measured for the OPD operated at a forward bias of 18 V using a 376-nm light source. A responsivity of 12.94 A/W, EQE of 2454%, and a D^* of 9.85×10^{12} Jones were obtained for the dual-mode OPD, operated at a reverse bias of −45 V, in the presence of long-wavelength light. The locations of the peak responses measured for the dual-mode

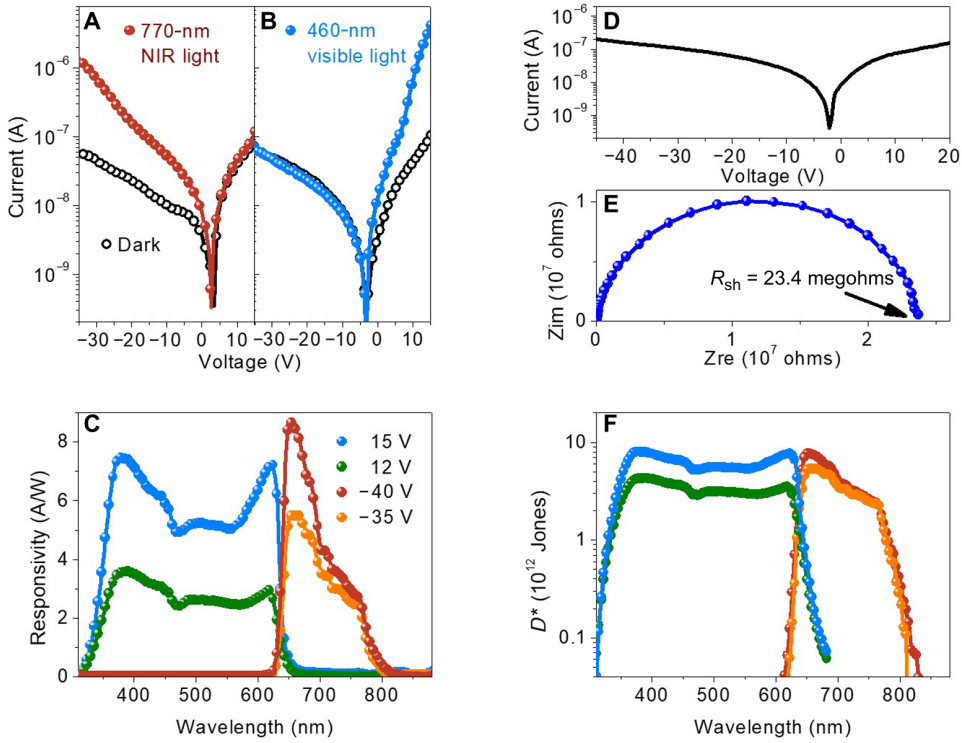

Fig. 4. Photo response characteristics. *I-V* characteristics measured for the dual-mode OPD in the presence of (**A**) NIR light (770 nm) and (**B**) visible light (460 nm) sources. (**C**) Responsivity spectra measured for the dual-mode OPD in the NIR light detection mode, operated at two different reverse biases of −35 and −40 V, and in the visible light detection mode, operated at two different forward biases of 12 and 15 V. (**D**) *I-V* characteristics measured for the OPD in the absence of light, averaged from more than seven measurements. (**E**) Impedance spectrum of the OPD revealing a shunt resistant of 23.4 megohms, measured at 10 V. (**F**) D^* of the dual-mode OPD operating in the NIR and visible light detection modes.

OPD in the NIR mode and visible light mode are associated with the PM process in the OPDs and do not overlap with the locations of the peak absorptions measured for the discrete binary blend P3HT:$PC_{70}BM$ (100:1) layer and ternary blend P3HT:PTB7-Th:$PC_{70}BM$ (70:30:1) layer, as shown in Fig. 2A.

Device physics

To understand the unique spectral responses of the trilayer PM OPD, we analyzed the distinct dual-mode NIR light and visible light detection phenomena of the OPD operated at the reverse and forward biases. The miscible $PC_{70}BM$ molecules distributed in the binary blend P3HT:$PC_{70}BM$ (100:1) visible light–absorbing layer and ternary blend P3HT:PTB7-Th:$PC_{70}BM$ (70:30:1) NIR light–absorbing layer act as the electron traps in the trilayer PM OPD. The tunneling hole injection occurs at the organic/cathode interface in the dual-mode OPD operated at a reverse bias due to the band bending that is induced by the high density of NIR light–generated electrons, as shown in Fig. 5A. At a reverse bias, however, the electron injection at the PFN-Br–modified ITO/P3HT:$PC_{70}BM$ (100:1) interface is suppressed due to the presence of a large energy barrier. In the presence of the visible light, no photogenerated electrons can be trapped by the $PC_{70}BM$ molecules in the NIR light–absorbing layer. Hence, no photocurrent is generated in the dual-mode OPD, as illustrated in Fig. 5B. This is because the visible light is absorbed only in the binary blend P3HT:$PC_{70}BM$ (100:1) visible light–absorbing layer and is fully depleted by the P3HT optical spacer, as depicted in Fig. 3B, leading to the formation of the trapped photogenerated electrons at the PFN-Br–modified ITO/P3HT:$PC_{70}BM$ (100:1) interface. Therefore, the dual-mode OPD responds only to the NIR light functioning as an NIR light OPD when it is operated at a reverse bias.

At a forward bias, the hole injection behavior in the dual-mode OPD is very different as compared to the OPD that is operated at a reverse bias in the presence of the NIR light, as illustrated in Fig. 5C. At a forward bias, the electron injection at the P3HT:PTB7-Th:$PC_{70}BM$ (70:30:1)/Al interface is suppressed due to the existence of a large interfacial energy barrier. The hole injection at the PFN-Br–modified ITO/P3HT:$PC_{70}BM$ (100:1) interface is suppressed due to the high interfacial energy barrier. In the presence of the visible light, the tunneling hole injection takes place at the PFN-Br–modified ITO/P3HT:$PC_{70}BM$ (100:1) interface in the dual-mode OPD at a forward bias due to the band bending that is caused by the high density of visible light–generated electrons, as shown in Fig. 5D. Hence, the dual-mode OPD only responds to the visible light serving as a visible light OPD operated at a forward bias.

Device performance

The linear dynamic range (LDR), defined as the linear light intensity dependence of the photocurrent in an OPD, of the dual-mode OPD in the presence of the NIR and visible light was analyzed. The LDR can be analyzed using the following equation

$$\mathrm{LDR} = 20\log\frac{I_{\mathrm{upper}}}{I_{\mathrm{lower}}} \quad (4)$$

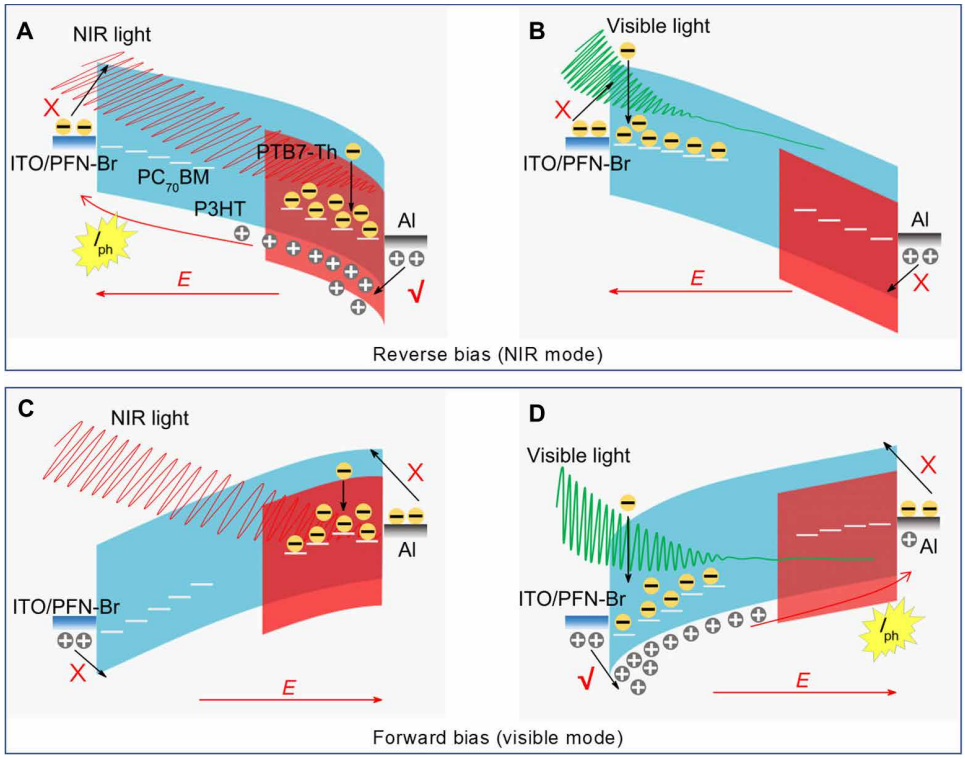

Fig. 5. Device physics. Schematic diagrams illustrating the working principles of the dual-mode OPD operated at a reverse bias (in the NIR light detection mode): (**A**) producing a photocurrent in the presence of the NIR light as a result of the efficient tunneling hole injection, enabled by the accumulation of the trapped photogenerated electrons at the P3HT:PTB7-Th:$PC_{70}BM$ (70:30:1)/Al interface, and (**B**) without generating photocurrent in the presence of the visible light due to the absence of the hole injection at the P3HT:PTB7-Th:$PC_{70}BM$ (70:30:1)/Al interface. The OPD operated at a forward bias (in the visible light detection mode): (**C**) without generating photocurrent due to a large hole injection barrier at the anode/P3HT:$PC_{70}BM$ (100:1) interface in the presence of NIR light, and (**D**) generating a photocurrent due to the enhanced tunneling hole injection, enabled by the accumulation of the photogenerated electrons at the anode/P3HT:$PC_{70}BM$ (100:1) interface in the presence of the visible light.

where I_{upper} and I_{lower} are the maximum and minimum limits of the intensity of light that the photocurrent of an OPD follows a linear dependence on light intensity (*24*). LDR characteristics measured for the dual-mode OPD in the NIR light detection mode, e.g., operated at different reverse biases of −20, −25, and −30 V using an NIR light-emitting diode (LED) light (770 nm) source over the NIR light intensity range from 10^{-9} to 10^{-1} W/cm^2, are plotted in Fig. 6A. An LDR of 120 dB was obtained for the dual-mode OPD operated in the NIR light detection mode. The photocurrent of the OPD deviates from the linear light intensity dependence when the NIR light intensity was below 10^{-8} W/cm^2. The LDR characteristics of the dual-mode OPD operated at different forward biases of 9, 12, and 15 V, measured using a visible LED light (460 nm) source over the visible light intensity range from 10^{-7} to 10^{-1} W/cm^2, are plotted in Fig. 6B. The dual-mode OPD had an LDR of 92 dB and departed from the linear light intensity dependence when the intensity of the visible light was below 10^{-6} W/cm^2. The results reveal that the relatively stable LDR of 120 dB in the presence of NIR light and an LDR of 92 dB in the presence of the visible light were obtained for the dual-mode OPD operated in the NIR and visible light detection modes.

Time-dependent photo responses of the dual-mode OPD measured in the presence of the NIR light (770 nm) and visible light (460 nm) sources are shown in Fig. 6C. In the measurement, the dual-mode OPD was biased at −35 or 15 V and exposed to a 0.1-Hz frequency modulated monochromatic light source. A schematic diagram illustrating the setup for the measurement of the dual-mode OPD is shown in fig. S4. The pictures were taken for the device, showing the layout of the cathode, anode, and active region of the dual-mode OPD. During the first 4 min, the dual-mode OPD was biased at −35 V and exposed to the modulated NIR light (770 nm) source, establishing a stable photo response to the NIR light. Then, the 0.1-Hz frequency modulated NIR light source was replaced with a 0.1-Hz frequency modulated visible light (460 nm) source. The photocurrent of the reverse-biased OPD decreased to zero when the visible light source was replaced for the NIR light source, as shown in Fig. 6C, indicating its insensitive nature to the visible light when it is operated in its NIR light detection mode. This shows that the dual-mode OPD, operated at a reverse bias of −35 V, is only sensitive to the NIR light, and it does not respond to the visible light. When the dual-mode OPD was operated at a forward bias (15 V), it responded only to the visible light with almost no photo response to the NIR light. The time-dependent photo response results confirm that the dual-mode OPD developed in this work has a unique feature of high NIR light response, operated at a reverse bias, and high visible light response, operated at a forward bias.

DISCUSSION

It is a great challenge to achieve a high-performing bias-switchable spectral response OPD in two distinct NIR and visible light bands. In this work, a dual-mode OPD, comprising a trilayer organic stack of visible light absorber/optical spacer/NIR light absorber, has been

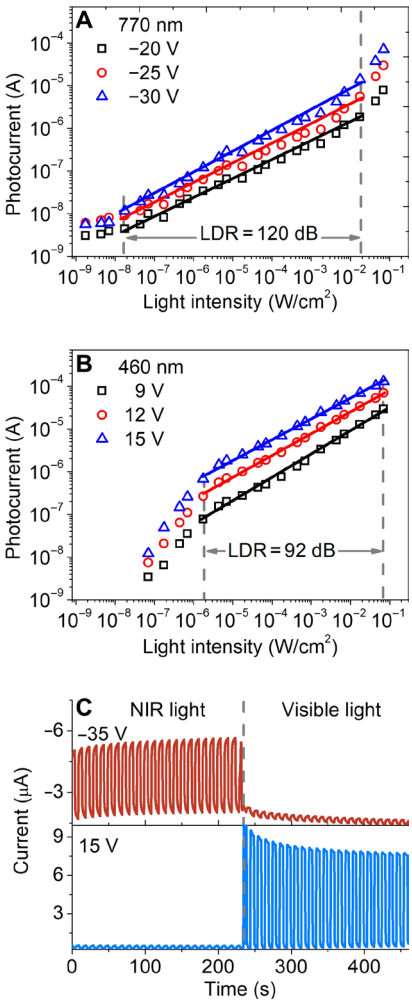

Fig. 6. Photodetection to NIR and visible light. LDR characteristics measured for the dual-mode OPD operated in the presence of (**A**) NIR light (770 nm) and (**B**) visible light (460 nm) sources at different reverse and forward biases. (**C**) Time-dependent photoresponses measured for a dual-mode OPD operated in the presence of the NIR light (770 nm) and visible light (460 nm) sources.

proposed. Such a trilayer PM OPD gives rise to the remarkable dual-mode light detection phenomena, exhibiting an NIR response operated at a reverse bias and a visible response at a forward bias. The dual-mode OPD is composed of a solution-processed 300-nm-thick binary blend P3HT:$PC_{70}BM$ (100:1) visible light–absorbing layer, a 320-nm-thick pristine P3HT optical spacer layer, and a 500-nm-thick ternary blend P3HT:PTB7-Th:$PC_{70}BM$ (70:30:1) NIR light–absorbing layer. The bias-switchable NIR and visible light responses in the dual-mode OPD are closely associated with two factors: (i) different distributions of the photogenerated electrons in the presence of the NIR and visible light and (ii) the bias polarity–dependent charge injection behaviors. In the presence of NIR light, the tunneling hole injection occurs at the NIR light absorber/cathode interface in the OPD operated at a reverse bias due to the band bending that is induced by the high density of the NIR light–generated electrons. In the presence of visible light, the tunneling hole injection takes place at the anode/visible light absorber interface in the OPD at a forward bias due to the band bending that is caused by the high density of visible light–generated electrons. A high responsivity of >10 A/W was obtained for the dual-mode OPD at two distinct short and long wavelengths. The dual-mode OPD developed in this work has a simultaneous high D^* of ~10^{13} Jones in both NIR and visible light bands.

The proposed trilayer dual-mode photodetectors may also be designed for photodetection over different short-wavelength light and long-wavelength light ranges using a combination of materials with desired absorption properties. Essentially, the use of an optical spacer in the trilayer enables the long-wavelength and short-wavelength parts of the incident light being absorbed selectively in the long-wavelength light– and short-wavelength light–absorbing regions. An appropriate optical spacer can be selected to deplete the short-wavelength light and enable the long-wavelength light reaching to the long-wavelength light–absorbing layer. Therefore, the trilayer OPD concept described in this work can be adopted for making different dual-mode photodetectors. The rapid progress made in the development of organic semiconducting materials offers an attractive option and a variety of material choices for application in different dual-mode photodetectors, e.g., a blue light and red light dual-mode OPD.

The trilayer dual-mode OPD presented in this work has a relatively thicker active layer of 1100 nm, which may induce a relatively high operation voltage. The driving voltage of the trilayer voltage may be reduced by selecting an appropriate material combination and interfacial engineering to reduce the charge injection barrier at the organic/electrode interfaces. It is anticipated that the active materials with well-defined narrow absorption spectrum in the respective short-wavelength and long-wavelength ranges would be ideal for application in trap-assisted dual-mode OPDs. In such a case, only a thin optical spacer is required to realize the distinct dual-mode detection, attaining a low driving voltage dual-mode OPDs.

High-performing dual-mode OPDs are an attractive alternative optical detection technology to the conventional single-mode OPDs. They offer additional advantages such as having a bias-switchable spectral response for applications in environmental pollution detection, wellness, and security monitoring in two distinct bands. The solution-processable fabrication processes also lead to significant cost-benefits, thereby creating next-generation large-area and flexible OPDs. The unique dual-mode light response properties demonstrated in this work offer an attractive option for new OPD concept and applications.

MATERIALS AND METHODS

Device fabrication

The binary P3HT:$PC_{70}BM$ solution was formulated by dissolving the P3HT:$PC_{70}BM$ mixture, with a weight ratio of P3HT to $PC_{70}BM$ of 100:1, in 1,2-dichlorobenzene (*o*-DCB). The ternary P3HT:PTB7-Th:$PC_{70}BM$ solution was formulated by dissolving the P3HT:PTB7-Th:$PC_{70}BM$ mixture in a weight ratio of P3HT to PTB7-Th to $PC_{70}BM$ of 70:30:1 in *o*-DCB. The prepatterned ITO glass substrates with a sheet resistance of 10 ohms per square were cleaned by ultrasonication sequentially with diluted liquid detergent, deionized water, acetone, and 2-propanol each for 30 min and dried by nitrogen gas flow. The wet-cleaned ITO/glass substrates were subjected to the UV-ozone treatment for 15 min before loading into the glove box, with O_2 and H_2O levels <0.1 parts per million, for device fabrication. The ITO surface was modified by an ultrathin PFN-Br layer, prepared by spin coating at a rotation speed of 3000 rpm for 50 s followed by annealing at 90°C for 10 min. The use of PFN-Br–modified ITO anode is to create an interface dipole (*25*), assisting in bidirectional tunneling hole injection in the PM OPD. Then, a 300-nm-thick binary blend layer of P3HT:

$PC_{70}BM$ (100:1) was deposited on the PFN-Br–modified ITO/glass substrates by spin coating at a rotation speed of 400 rpm for 100 s and annealing at 80°C for 20 s. A 320-nm-thick pristine P3HT optical spacer and a 500-nm-thick ternary blend layer of P3HT:PTB7-Th:$PC_{70}BM$ (70:30:1) were first coated on the precleaned silicon (Si) wafers, respectively. A 320-nm-thick pristine P3HT optical spacer was then transferred onto the surface of the binary blend P3HT:$PC_{70}BM$ (100:1) visible light–absorbing layer by lamination transfer using a polydimethylsiloxane (PDMS) mold, forming a bilayer P3HT:$PC_{70}BM$ (100:1) (300 nm)/P3HT (320 nm) structure. A 500-nm-thick P3HT:PTB7-Th:$PC_{70}BM$ (70:30:1) NIR light–absorbing layer was then overlaid on the surface of the bilayer P3HT:$PC_{70}BM$ (100:1) (300 nm)/P3HT (320 nm) structure using the same lamination transfer process, forming a trilayer configuration active layer of P3HT:$PC_{70}BM$ (100:1) (300 nm)/P3HT (320 nm)/P3HT:PTB7-Th:$PC_{70}BM$ (70:30:1) (500 nm) on the PFN-Br–modified ITO/glass substrate. The use of the PDMS lamination approach is to avoid the damage to the underlying organic materials in the trilayer configuration organic active layer if it were formed by the full-solution process, as the same *o*-DCB solvent was used in the binary P3HT:$PC_{70}BM$, pristine P3HT, and ternary P3HT:PTB7-Th:$PC_{70}BM$ solutions. The multilayer samples were then transferred to the adjacent vacuum chamber, with a base pressure of 5×10^{-4} Pa for deposition of a 100-nm-thick Al electrode. The OPDs has an active area of 2.0 mm by 2.0 mm, defined by the overlapping area between the front ITO anode and the upper Al cathode.

Lamination transfer method

The organic stack of P3HT:$PC_{70}BM$ (100:1) (300 nm)/P3HT (320 nm)/P3HT:PTB7-Th:$PC_{70}BM$ (70:30:1) (500 nm) films was fabricated by transfer process using a flat PDMS mold. A 1-mm-thick flat PDMS mold, with an area of 25 mm by 25 mm, was prepared using the PDMS solution, formulated by mixing the elastomer and curing agent solution in a weight ratio of 10:1. A 300-nm-thick binary blend P3HT:$PC_{70}BM$ (100:1) visible light–absorbing layer was deposited on the glass/ITO/PFN-Br substrates by spin coating. A 320-nm-thick pristine P3HT optical spacer layer and a 500-nm-thick ternary blend P3HT:PTB7-Th:$PC_{70}BM$ (70:30:1) NIR light–absorbing layer were coated on the Si wafers separately. A flat PDMS mold was then pressed on the surface of the organic layer/Si wafer, the sample was dipped in the distilled water for 1 min, and then the Si wafer was removed carefully, leaving the organic layer on the flat PDMS mold. The transfer of the P3HT layer was done by pressing the P3HT-coated PDMS mold on the surface of the P3HT:$PC_{70}BM$ (100:1) (300 nm)/PFN-Br/ITO/glass substrate in the glovebox, followed by an annealing for 15 min, then the flat PDMS mold was removed carefully, forming a bilayer P3HT (320 nm)/P3HT:$PC_{70}BM$ (100:1) (300 nm) stack on the PFN-Br–modified ITO/glass substrate. Next, the transfer of the P3HT:PTB7-Th:$PC_{70}BM$ (70:30:1) layer was done by pressing the P3HT:PTB7-Th:$PC_{70}BM$ (70:30:1)–coated PDMS mold on the surface of the P3HT (320 nm)/P3HT:$PC_{70}BM$ (100:1) (300 nm)/PFN-Br/ITO/glass substrate, followed by annealing for 15 min, then the flat PDMS mold was removed carefully, forming a trilayer organic stack of P3HT:$PC_{70}BM$ (100:1) (300 nm)/P3HT (320 nm)/P3HT:PTB7-Th:$PC_{70}BM$ (70:30:1) (500 nm) on PFN-Br–modified ITO/glass substrate.

Optical simulation

The optical field distribution and profile of the photogenerated charge carriers in the OPDs were simulated using the optical admittance analyses. The wavelength-dependent refractive indexes, $n(\lambda)$, and extinction coefficients, $k(\lambda)$, of the pristine P3HT layer, binary blend P3HT:$PC_{70}BM$ (100:1) layer, and ternary blend P3HT:PTB7-Th:$PC_{70}BM$ (70:30:1) layer were measured by the dual rotating-compensator Mueller matrix ellipsometer (ME-L ellipsometer, Wuhan Eoptics Technology Co.). $n(\lambda)$ and $k(\lambda)$ obtained for the corresponding pristine P3HT layer, binary blend P3HT:$PC_{70}BM$ (100:1) layer, and ternary blend P3HT:PTB7-Th:$PC_{70}BM$ (70:30:1) are plotted in fig. S6. The charge generation rate in the trilayer configuration organic active layer was estimated using the following equation

$$G(\lambda) \propto \frac{\alpha(\lambda)}{h\nu} \times \eta \tag{5}$$

where $G(\lambda)$ is the density of the photogenerated charge carriers, $\alpha(\lambda)$ is the absorbance of the active layer, h is the Plank constant, ν is the photon frequency, and η is the exciton dissociation efficiency. As an approximation, a constant η across the active layer was adopted in the calculation.

Characterizations

The *I*-*V* characteristics of the OPDs were measured by a KEITHLEY 2614B source meter. Two LED light sources with the different peak emission wavelengths of 770 nm (NIR light) and 460 nm (visible light), driven by a RIGOL DG4102 function generator, were used for measuring the NIR and visible light responses of the dual-mode OPDs. The intensity of the NIR and visible light sources was controlled using a set of neutral optical filters. EQE, defined as the ratio of the number of the photogenerated charge carriers to the number of the incident photons, was calculated using the following equation

$$\mathrm{EQE} = \frac{(I_l - I_d)/e}{P_{in}/h\nu} \tag{6}$$

where I_l and I_d are the photocurrent and dark current, e is the elementary electron charge (1.6×10^{-19} C), and P_{in} is the power of the incident light. The monochromatic light source used in EQE measurement was generated by a Xenon lamp and the Bentham TMc300 monochromator. Transient photoresponses of the dual-mode OPDs were measured using a Tektronix OPD2022B digital phosphor oscilloscope. The dc bias used in the transient photoresponses measurements was controlled by the RIGOL DP821A dc power supply.

Single-carrier devices

The hole mobility (μ_h) and electron mobility (μ_e) of the P3HT:$PC_{70}BM$ (100:1)– and P3HT:PTB7-Th:$PC_{70}BM$ (70:30:1)–based single-carrier devices were analyzed using the space charge–limited current technique. The typical $J^{0.5}$-*V* characteristics measured for the hole-only devices ITO/PEDOT:PSS/P3HT:$PC_{70}BM$ (100:1)/Au (blue circles) and ITO/PEDOT:PSS/ P3HT:PTB7-Th:$PC_{70}BM$ (70:30:1)/Au (red triangles) are shown in fig. S5A. The $J^{0.5}$-*V* characteristics measured for the electron-only devices ITO/ZnO/P3HT:$PC_{70}BM$ (100:1)/LiF/Al (blue circles) and ITO/ZnO/P3HT:PTB7-Th:$PC_{70}BM$ (70:30:1)/LiF/Al (red triangles) are plotted in fig. S5B. The μ_h obtained using the hole-only devices of ITO/PEDOT:PSS/P3HT:$PC_{70}BM$ (100:1)/Au and ITO/PEDOT:PSS/P3HT:PTB7-Th:$PC_{70}BM$ (70:30:1)/Au is in the order of 10^{-5} cm^2/Vs, which is much higher than μ_e obtained for the electron-only devices of ITO/ZnO/P3HT:$PC_{70}BM$ (100:1)/LiF/Al and ITO/ZnO/P3HT:PTB7-Th:$PC_{70}BM$ (70:30:1)/LiF/Al (10^{-10} cm^2/Vs). The hole mobility and electron mobility results agree well with previous

report (*26*). The charge transport mobility measurement reveals the electron trapping nature of the binary blend P3HT:$PC_{70}BM$ (100:1) and ternary blend P3HT:PTB7-Th:$PC_{70}BM$ (70:30:1) organic active layers in the PM OPDs.

SUPPLEMENTARY MATERIALS

Supplementary material for this article is available at http://advances.sciencemag.org/cgi/content/full/6/5/eaaw8065/DC1

Fig. S1. Bias polarity–dependent spectral responses of a P3HT:PTB7-Th:$PC_{70}BM$ (70:30:1)–based PM OPD.

Fig. S2. Schematic energy level diagram of the functional materials used in the dual-mode OPDs.

Fig. S3. EQE spectra measured for the trilayer dual-mode OPD at different reverse and forward biases.

Fig. S4. A schematic diagram illustrating the setup for the measurement of the dual-mode OPD.

Fig. S5. Charge transport properties of the P3HT:$PC_{70}BM$ (100:1)– and P3HT:PTB7-Th:$PC_{70}BM$ (70:30:1)–based single-carrier devices were analyzed using the space charge–limited current technique.

Fig. S6. Optical constants of the functional layers used in the optical simulation in this work.

Table S1. Summarized photodetection parameters.

REFERENCES AND NOTES

1. F. P. García de Arquer, A. Armin, P. Meredith, E. H. Sargent, Solution-processed semiconductors for next-generation photodetectors. *Nat. Rev. Mater.* **2**, 16100 (2017).
2. N. Li, Z. Lan, L. Cai, F. Zhu, Advances in solution-processable near-infrared phototransistors. *J. Mater. Chem. C* **7**, 3711–3729 (2019).
3. N. Li, W. Lan, Y. S. Lau, L. Cai, A. A. Syed, F. Zhu, Enhanced long wavelength omnidirectional photoresponses in photonic-structured perovskite photodetectors. *J. Mater. Chem. C* **7**, 9573–9580 (2019).
4. F. Yan, H. Liu, W. Li, B. Chu, Z. Su, G. Zhang, Y. Chen, J. Zhu, D. Yang, J. Wang, Double wavelength ultraviolet light sensitive organic photodetector. *Appl. Phys. Lett.* **95**, 253308 (2009).
5. Z. Wu, W. Yao, A. E. London, J. D. Azoulay, T. N. Ng, Temperature-dependent detectivity of near-infrared organic bulk heterojunction photodiodes. *ACS Appl. Mater. Interfaces* **9**, 1654–1660 (2017).
6. N. Li, Y. S. Lau, Z. Xiao, L. Ding, F. Zhu, NIR to visible light upconversion devices comprising an NIR charge generation layer and a perovskite emitter. *Adv. Opt. Mater.* **6**, 1801084 (2018).
7. K. H. An, B. O'Connor, K. P. Pipe, M. Shtein, Organic photodetector with spectral response tunable across the visible spectrum by means of internal optical microcavity. *Org. Electron.* **10**, 1152–1157 (2009).
8. A. Armin, R. D. Jansen-van Vuuren, N. Kopidakis, P. L. Burn, P. Meredith, Narrowband light detection via internal quantum efficiency manipulation of organic photodiodes. *Nat. Commun.* **6**, 6343 (2015).
9. Q. Lin, A. Armin, P. L. Burn, P. Meredith, Filterless narrowband visible photodetectors. *Nat. Photonics* **9**, 687–694 (2015).
10. Y. Fang, Q. Dong, Y. Shao, Y. Yuan, J. Huang, Highly narrowband perovskite single-crystal photodetectors enabled by surface-charge recombination. *Nat. Photonics* **9**, 679–686 (2015).
11. Z. Tang, Z. Ma, A. Sánchez-Díaz, S. Ullbrich, Y. Liu, B. Siegmund, A. Mischok, K. Leo, M. Campoy-Quiles, W. Li, K. Vandewal, Polymer:fullerene bimolecular crystals for near-infrared spectroscopic photodetectors. *Adv. Mater.* **29**, 1702184 (2017).
12. W. Wang, F. Zhang, M. Du, L. Li, M. Zhang, K. Wang, Y. Wang, B. Hu, Y. Fang, J. Huang, Highly narrowband photomultiplication type organic photodetectors. *Nano Lett.* **17**, 1995–2002 (2017).
13. B. Siegmund, A. Mischok, J. Benduhn, O. Zeika, S. Ullbrich, F. Nehm, M. Böhm, D. Spoltore, H. Fröb, C. Korner, K. Leo, K. Vandewal, Organic narrowband near-infrared photodetectors based on intermolecular charge-transfer absorption. *Nat. Commun.* **8**, 15421 (2017).
14. M. I. Saidaminov, M. A. Haque, M. Savoie, A. L. Abdelhady, N. Cho, I. Dursun, U. Buttner, E. Alarousu, T. Wu, O. M. Bakr, Perovskite photodetectors operating in both narrowband and broadband regimes. *Adv. Mater.* **28**, 8144–8149 (2016).
15. L. Li, F. Zhang, W. Wang, Q. An, J. Wang, Q. Sun, M. Zhang, Trap-assisted photomultiplication polymer photodetectors obtaining an external quantum efficiency of 37500%. *ACS Appl. Mater. Interfaces* **7**, 5890–5897 (2015).
16. L. Li, F. Zhang, J. Wang, Q. An, Q. Sun, W. Wang, J. Zhang, F. Teng, Achieving EQE of 16,700% in P3HT:$PC_{71}BM$ based photodetectors by trap-assisted photomultiplication. *Sci. Rep.* **5**, 9181 (2015).
17. L. Li, F. Zhang, W. Wang, Y. Fang, J. Huang, Revealing the working mechanism of polymer photodetectors with ultra-high external quantum efficiency. *Phys. Chem. Chem. Phys.* **17**, 30712–30720 (2015).
18. J. Miao, F. Zhang, M. Du, W. Wang, Y. Fang, Photomultiplication type narrowband organic photodetectors working at forward and reverse bias. *Phys. Chem. Chem. Phys.* **19**, 14424–14430 (2017).
19. J. Miao, F. Zhang, M. Du, W. Wang, Y. Fang, Photomultiplication type organic photodetectors with broadband and narrowband response ability. *Adv. Opt. Mater.* **6**, 1800001 (2018).
20. W. Lan, Y. Wang, J. Singh, F. Zhu, Omnidirectional and broadband light absorption enhancement in 2-D photonic-structured organic solar cells. *ACS Photon.* **5**, 1144–1150 (2018).
21. Z. Wu, B. Wu, H. L. Tam, F. Zhu, An insight on oxide interlayer in organic solar cells: From light absorption and charge collection perspectives. *Org. Electron.* **31**, 266–272 (2016).
22. Z. Wu, W. Yao, A. E. London, J. D. Azoulay, T. N. Ng, Elucidating the detectivity limits in shortwave infrared organic photodiodes. *Adv. Funct. Mater.* **28**, 1800391 (2018).
23. J. Miao, F. Zhang, Y. Lin, W. Wang, M. Gao, L. Li, J. Zhang, X. Zhan, Highly sensitive organic photodetectors with tunable spectral response under bi-directional bias. *Adv. Opt. Mater.* **4**, 1711–1717 (2016).
24. C. Bao, Z. Chen, Y. Fang, H. Wei, Y. Deng, X. Xiao, L. Li, J. Huang, Low-noise and large-linear-dynamic-range photodetectors based on hybrid-perovskite thin-single-crystals. *Adv. Mater.* **29**, 1703209 (2017).
25. L. Chen, M.-H. Lee, Y. Wang, Y. S. Lau, A. A. Syed, F. Zhu, Interface dipole for remarkable efficiency enhancement in all-solution-processable transparent inverted quantum dot light-emitting diodes. *J. Mater. Chem. C* **6**, 2596–2603 (2018).
26. C. H. Y. Ho, S. H. Cheung, H.-W. Li, K. L. Chiu, Y. Cheng, H. Yin, M. H. Chan, F. So, S.-W. Tsang, S. K. So, Using ultralow dosages of electron acceptor to reveal the early stage donor-acceptor electronic interactions in bulk heterojunction blends. *Adv. Energy Mater.* **7**, 1602360 (2017).

Acknowledgments: The optical constants of the ternary blend P3HT:PTB7-Th:$PC_{70}BM$ (70:30:1) and binary blend P3HT:$PC_{70}BM$ (100:1) layers were measured by H.-L. Yip and R. Xia at South China University of Technology. **Funding:** This work was financially supported by the Research Grants Council, University Grants Committee, Hong Kong, General Research Fund (GRF/12302817), Hong Kong Baptist University Inter-institutional Collaborative Research Scheme (RC-ICRS/15-16/04), and State Key Laboratory of Environmental and Biological Analysis (SKLP_1920_P04). **Author contributions:** F.Z. and D.L. cosupervised the graduate student, Z.L., who carried out most of the experiments (OPD fabrication/characterization). Y.L. helped Z.L. for the device simulation. W.K.E.C. helped Z.L. for the device characterization. S.C. helped Z.L. in the device fabrication. F.Z. directed the overall project. The manuscript was written with contributions from all authors. **Competing interests:** F.Z. and Z.L. are inventors on patent applications related to this work filed by Hong Kong Baptist University (US 16,592,793, filed 4 October 2019, China no. 201910951975.5, and Japan no. 2019-185194, filed 8 October 2019). The authors declare no other competing interests. **Data and materials availability:** All data needed to evaluate the conclusions in the paper are present in the paper and/or the Supplementary Materials. Additional data related to this paper may be requested from the authors.

Submitted 26 January 2019
Accepted 20 November 2019
Published 31 January 2020
10.1126/sciadv.aaw8065

Citation: Z. Lan, Y. Lei, W. K. E. Chan, S. Chen, D. Luo, F. Zhu, Near-infrared and visible light dual-mode organic photodetectors. *Sci. Adv.* **6**, eaaw8065 (2020).